

## Chapter 2

# Theory

Let us look at the theoretical principles of XPCS and outline the connection of the actual measurements to the conclusions which can be drawn from them. We will see how intensity patterns arise from scattering at atoms, how these patterns over time can be interpreted to give information on correlations on atoms in real space and how these correlations can be interpreted to give insight into actual atomic movements. Finally we will look at some additional considerations on this method applied to the atomic dynamics in glasses.

### 2.1 Achieving Coherent Scattering

Crucial to any XPCS experiment is coherently scattered radiation. Let us see how scattering can be achieved in general, how sufficient intensities are reached and how coherence can be ensured.

#### 2.1.1 *Scattering Intensity and Speckle Patterns*

When an at least partly coherent monochromatic beam of light scatters at a grid or an ensemble of slits or particles, a scattering pattern can be observed at a screen put downstream the propagation direction of the beam (see Fig. 2.1). This pattern is static if nothing changes in the setup and particularly as long as the grid stays unchanged. If the spacing of the grid is modified or parts of the grid are removed, then the scattering pattern will change accordingly. There is normally no straightforward way to directly deduce on the structure of a scatterer from the diffraction pattern. However, under certain circumstances it is possible to gain information on the changes in the structure from the time evolution of scattering intensity. This is the underlying principle of XPCS.

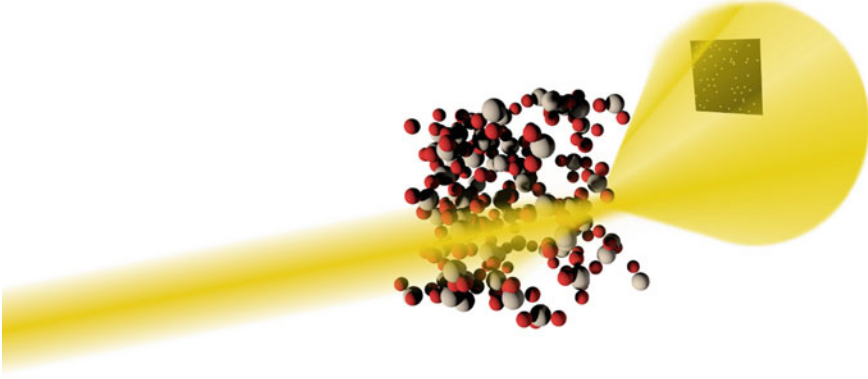


**Fig. 2.1** Visualisation of X-rays scattered at an atomic arrangement. The detector on the right catches part of the scattered radiation

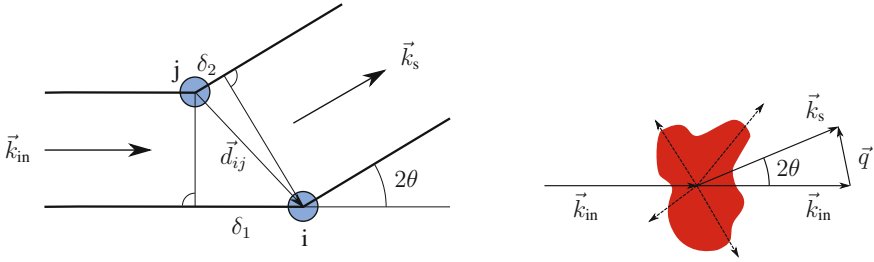


**Fig. 2.2** Schematic of the scattering process in matter. *Left* The incident radiation with wave vector  $\vec{k}_{\text{in}}$  is scattered at two atoms  $i$  and  $j$ . When observing the scattered radiation at angle  $2\theta$ , the scattered waves have a path difference of  $\delta = \delta_1 - \delta_2$ . *Right* The scattered radiation in the sample can be described in terms of the difference of the wave vectors of the incident radiation  $\vec{k}_{\text{in}}$  and the scattered radiation  $\vec{k}_s$ , denoted as  $\vec{q}$

The scattering pattern of coherent radiation is also called speckle pattern. This results from the fact that for elastically scattered radiation only the phases change but the frequencies stay the same, so by constructive and destructive interference a pattern is created which contains areas of different intensity. A schematic is shown in Fig. 2.2. Two waves scattered at different atoms under an angle  $2\theta$  will have a path difference of  $\delta = \delta_1 - \delta_2$ . This can be expressed in terms of the vector between the two scattering centres  $\vec{d}_{ij}$  and the wave vectors. With the projections of  $\vec{d}_{ij}$  on the wave vectors,  $\vec{d}_{ij} \cdot \vec{k}_{\text{in}} = \delta_1$  and  $\vec{d}_{ij} \cdot \vec{k}_s = \delta_2$  and with the position vectors to the scattering centres in an arbitrary basis  $\vec{r}_i - \vec{r}_j = \vec{d}_{ij}$ , the path difference can be described as

$$\delta = \vec{q} \cdot (\vec{r}_i - \vec{r}_j). \quad (2.1)$$

Here,  $\vec{q} = \vec{k}_{\text{in}} - \vec{k}_s$  is called the scattering vector. Its length depends on the scattering angle, as

$$\sin\left(\frac{2\theta}{2}\right) = \frac{q}{2k_{\text{in}}}. \quad (2.2)$$

With  $k_{\text{in}} = \frac{2\pi}{\lambda}$ , the length of the scattering vector can be expressed as

$$q = \frac{4\pi}{\lambda} \sin\left(\frac{2\theta}{2}\right). \quad (2.3)$$

Considering the Abbe limit in the form  $d = \frac{\lambda}{2\sin\theta}$ , with structure size  $d$ , wavelength  $\lambda$ , and scattering angle  $2\theta$  (up to about  $35^\circ$  in the experiments conducted in the course of this thesis) shows that in order to be sensitive for atomic distances, the wavelength of the radiation needs to be in the angstrom regime. In the synchrotron experiments reported here, radiation with a wavelength of about  $1.5 \text{ \AA}$  is used, which is equivalent to photon energies in the range of some 7–8 keV.

The intensity measured at a detector is the result of the interference of all waves scattered in the sample. We will restrict ourselves to elastic scattering (Rayleigh scattering), as only this type of scattering leads to the fixed phase relation of the scattered radiation required for XPCS. Thus the energy of the scattered radiation considered in the typical XPCS experiment is for all practical purposes unchanged. The electrical field far from the scattering centres is in principle the sum of all scattered waves

$$E(\vec{q}, t) \propto \sum_{i=1}^N a_i e^{i\vec{q}\vec{r}_i(t)}, \quad (2.4)$$

with number of atoms  $N$  and scattering length  $a_i$  (which is implicitly also dependent on the scattering vector). It can also be expressed as the Fourier transform of the electron density, thus containing the information on the electron positions and consequently on the atomic positions. Unfortunately, the oscillations of the electrical field are too fast to be directly accessible in the experiment (for an X-ray photon with an energy of  $h\nu \approx 8 \text{ keV}$  the oscillation frequency of the electromagnetic field is on the order of  $10^{18} \text{ s}^{-1}$ ). However, what is readily detectable is the intensity. The intensity is proportional to the time average of the squared electrical field  $EE^*$ :

$$I(\vec{q}) = \langle E(\vec{q}, t) E^*(\vec{q}, t) \rangle_t \propto \left\langle \sum_{i=1}^N \sum_{j=1}^N a_i a_j^* e^{i\vec{q}(\vec{r}_i(t) - \vec{r}_j(t))} \right\rangle_t \quad (2.5)$$

Thus the intensity is taking into account the different phases due to different path lengths. This can be expressed with the phase factor from Eq. (2.1) as interference factor

$$e^{i\delta} = e^{i\vec{q}(\vec{r}_i - \vec{r}_j)}. \quad (2.6)$$

This shows that the intensity pattern contains information on the structural details of the material. However, it is normally not directly possible to access these details

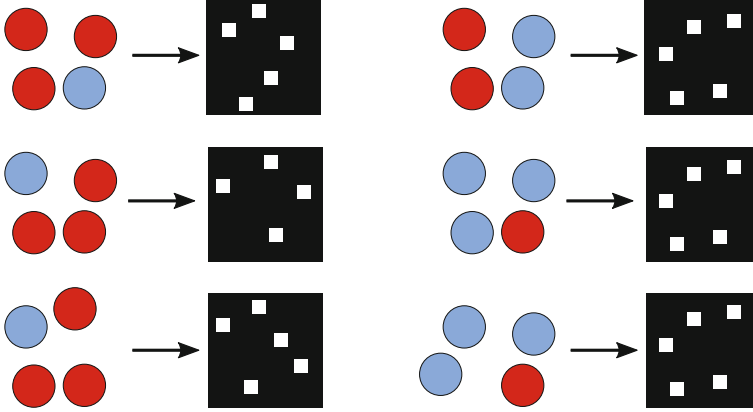


**Fig. 2.3** Sketch of atomic arrangements (with two different element species) and resulting scattering patterns. *Left* A change in atomic arrangement leads to a change in the scattering pattern. *Right* It is possible that different arrangements produce the same scattering pattern. Thus it is not possible to directly deduce the structure from the scattering pattern

due to the lost phase information by averaging, or in other words, there is no direct way to invert Eq. (2.5). This is widely known as the phase problem, as depicted in Fig. 2.3. There are different approaches to circumvent this problem, notably in X-ray imaging (Marchesini et al. 2003). When investigating dynamics, the structure of the material is not of direct concern, but rather the *changes* in structure. We can thus ignore the structural details and use the time fluctuations of the scattering pattern instead to study the dynamics of the material. This fact is utilised by the method of XPCS. The principles of this method can be derived based on the van Hove pair correlation function, as we will see in Sect. 2.2.1.

### 2.1.2 Optimal Scattering Thickness

For any scattering experiment, it is important to find the optimal sample thickness  $W$  for the given geometry. An analytical expression can be derived for the scattered intensity  $I$  at a scattering angle  $2\theta$  relative to the direct beam with the absorption coefficient  $\mu$  and the isotropic scattering factor  $s$ . Assuming the incident beam with intensity  $I_0$  to be perpendicular to the sample surface and integrating over the scattered intensity in an infinitesimal interval of the sample,

$$dI = I_0 e^{-\mu x} s e^{-\mu y} dx, \quad (2.7)$$

we get

$$I = I_0 s \int_0^W e^{-\mu(x+y)} dx. \quad (2.8)$$

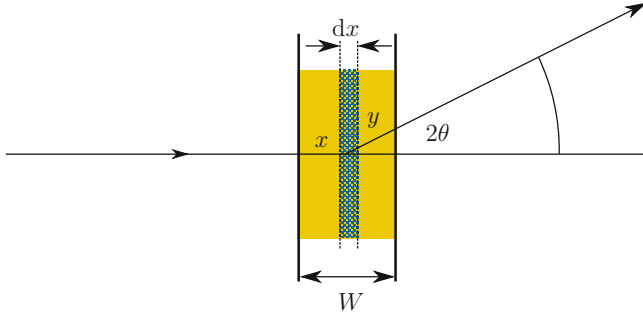


**Fig. 2.4** Derivation of optimal sample thickness  $W$  by integration over infinitesimal intervals of the path length  $dx$ , which is dependent on the scattering angle  $2\theta$

As can be seen from Fig. 2.4,  $y = \frac{W-x}{\cos 2\theta}$ , which leads to:

$$\begin{aligned} I &= I_0 s \int_0^W e^{-\mu(x + \frac{W-x}{\cos 2\theta})} dx \\ &= I_0 s \frac{e^{-\frac{\mu W}{\cos 2\theta}} - e^{-\mu W}}{\mu \left(1 - \frac{1}{\cos 2\theta}\right)} \end{aligned} \quad (2.9)$$

The optimum can be found for  $\frac{\partial I}{\partial W} = 0$  (and  $\frac{\partial^2 I}{\partial^2 W} < 0$ ):

$$\frac{\partial I}{\partial W} = I_0 s \left( -\frac{e^{-\frac{\mu W}{\cos 2\theta}}}{\cos 2\theta \left(1 - \frac{1}{\cos 2\theta}\right)} + \frac{e^{-\mu W}}{1 - \frac{1}{\cos 2\theta}} \right) = 0 \quad (2.10)$$

Thus we get

$$\begin{aligned} e^{-\mu W + \frac{\mu W}{\cos 2\theta}} &= \frac{1}{\cos 2\theta} \\ W &= \frac{\ln(\cos 2\theta)}{\mu \left(1 - \frac{1}{\cos 2\theta}\right)}. \end{aligned} \quad (2.11)$$

For small angles Eq. (2.11) can be further simplified by rewriting Eq. (2.9) and expanding the exponential:

$$\begin{aligned} I &= I_0 s e^{-\frac{\mu W}{\cos 2\theta}} \frac{1 - e^{-\mu W \left(1 - \frac{1}{\cos 2\theta}\right)}}{\mu \left(1 - \frac{1}{\cos 2\theta}\right)} \\ &\approx I_0 s e^{-\frac{\mu W}{\cos 2\theta}} \frac{\mu W \left(1 - \frac{1}{\cos 2\theta}\right)}{\mu \left(1 - \frac{1}{\cos 2\theta}\right)} \\ &= I_0 s W e^{-\frac{\mu W}{\cos 2\theta}} \end{aligned} \quad (2.12)$$

The optimum can be found analogously to Eq. (2.11). The calculation yields

$$W_{\text{small angles}} = \frac{\cos 2\theta}{\mu}. \quad (2.13)$$

This result is accurate with a relative deviation of less than 10 % for the angles which we will consider here.

The optimal thickness has been derived under the assumption that no multiple scattering occurs. While this is true for X-rays, it does not hold for other methods like neutron scattering. There, a lower sample thickness compared to Eq. (2.11) is necessary.

The thickness derived here is optimal for X-rays in that the amount of detected radiation is at a maximum at that thickness. However, the intensity is not the only factor which has to be considered in aXPCS. We will have to adjust the obtained result when taking coherence into account.

### 2.1.3 Coherence Properties

A very important property the scattered radiation must have is a high degree of coherence. We will later see that the Signal-to-Noise Ratio (SNR) is roughly proportional to the degree of coherence. The coherence properties of the incoming radiation can be characterised in terms of the longitudinal coherence length  $\xi_l$  and the transversal coherence length  $\xi_t$ . A detailed treatment of the criteria for coherent X-ray scattering can be found in Abernathy et al. (1998), Sandy et al. (1999) and Sutton (2006, 2008).

In order to have sufficient coherence in the scattered radiation, the scattered photons should not get out of phase while travelling on different optical paths through the sample. This can be achieved by having a maximum path length difference smaller than the longitudinal coherence length  $\xi_l$ . The radiation is not perfectly monochromatic. Typically, the wavelengths of the beam can be described by a spectral distribution with full width at half maximum  $\Delta\lambda$ . The longitudinal coherence length is defined as the distance after which radiation of wavelength  $\lambda$  is shifted by a phase of  $\pi$  (or in other words, half of a wavelength) from radiation of wavelength  $\lambda + \Delta\lambda$  (see Fig. 2.5). Solving

$$\left(N + \frac{1}{2}\right)\lambda = N(\lambda + \Delta\lambda) \quad (2.14)$$

for  $N$  gives

$$N = \frac{\lambda}{2\Delta\lambda}. \quad (2.15)$$

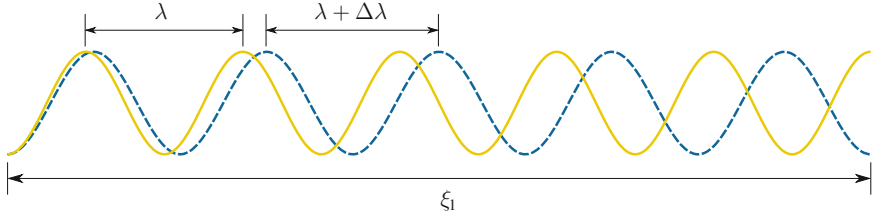


**Fig. 2.5** Visualisation of the longitudinal coherence length  $\xi_1$ . As the beam radiation is not perfectly monochromatic, there is a spread of wavelengths, the extent of which can be characterised by  $\Delta\lambda$ . The longitudinal coherence length  $\xi_1$  is defined as the distance after which radiation of wavelength  $\lambda$  is shifted by a phase of  $\pi$  from radiation of wavelength  $\lambda + \Delta\lambda$

With a typical monochromaticity of  $\frac{\Delta\lambda}{\lambda} \approx 10^{-4}$ ,  $N$  is much greater than 1 and

$$\xi_1 = \left(N + \frac{1}{2}\right) \lambda \approx N\lambda = \frac{\lambda^2}{2\Delta\lambda}. \quad (2.16)$$

The maximum path length difference is defined as the difference between the shortest and the longest geometrical path a photon of a beam with diameter  $d$  can travel through the sample with thickness  $W$  if being scattered under an angle  $2\theta$ . The two maximal paths are visualised in Fig. 2.6. The path length difference  $P$  is thus

$$P = p_1 + p_2 - p_3. \quad (2.17)$$

The sections of the paths can be derived from the geometrical relations

$$p_2 = (d + x) \sin 2\theta \quad (2.18)$$

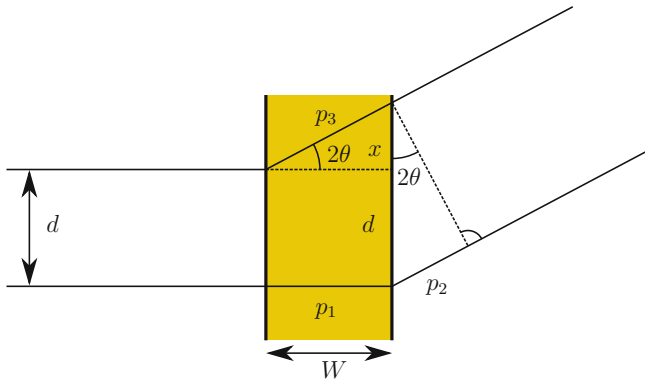


**Fig. 2.6** Derivation of the maximum path length difference. The beam with maximal span  $d$  is scattered in the sample. The maximum path length difference for a certain scattering angle  $2\theta$  is the geometrical path difference between a directly scattered photon and a photon getting scattered after passing the entire sample thickness  $W$

and

$$p_3 = \frac{W}{\cos 2\theta}. \quad (2.19)$$

With  $p_3 = W^2 + x^2$ , an expression for  $x$  can be found:

$$x = W \sqrt{\frac{1}{\cos^2 2\theta} - 1} = W \frac{\sin 2\theta}{\cos 2\theta} \quad (2.20)$$

Thus the maximum path length difference can be expressed as

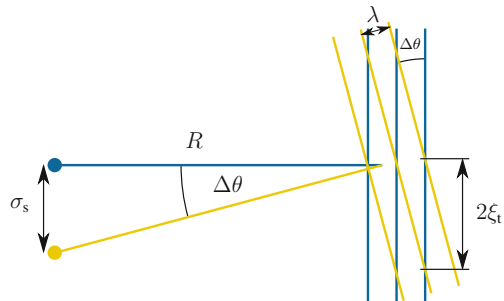
$$\begin{aligned} P &= d \sin 2\theta + W \left( 1 - \frac{1}{\cos 2\theta} \right) + W \frac{\sin^2 2\theta}{\cos 2\theta} \\ &= d \sin 2\theta + W \frac{\cos 2\theta - \cos^2 2\theta}{\cos 2\theta} \\ &= d \sin 2\theta + 2W \sin^2 \theta. \end{aligned} \quad (2.21)$$

As we can see, the path length difference depends on the beam diameter, the scattering angle and the sample thickness. The smaller the path length difference, the higher the coherence of the scattered radiation will be. Thus for a given scattering angle, the coherence decreases with increasing beam diameter and increasing sample thickness. This shows that the sample thickness will have to be a compromise between scattering intensity and coherence. For typical values of  $d \approx 10 \mu\text{m}$ ,  $2\theta \approx 35^\circ$  and  $W \approx 10 \mu\text{m}$ , we obtain a maximum path length difference of  $P \approx 7.5 \mu\text{m}$ .

Another condition for coherence is that the scattering centres should not be farther apart than the transversal coherence width perpendicular to the beam. This can be fulfilled by having the beam width in the order of the transversal coherence length  $\xi_t$ , which depends on the size  $\sigma_s$  and the distance  $R$  of the X-ray source. The transversal coherence length is defined to be the transversal distance within which two waves with the same wavelength originating from two points with distance  $\sigma_s$  will have a phase difference of  $\pi$ . From the geometrical considerations (see Fig. 2.7)

$$\sin \Delta\theta = \frac{\lambda}{2\xi_t} \quad (2.22)$$

**Fig. 2.7** Visualisation of the transversal coherence length  $\xi_t$ . Due to the angular beam divergence  $\Delta\theta$ , the waves originating from two points with distance  $\sigma_s$  will have a phase difference of  $\pi$  in a transversal distance which is defined to be the transversal coherence length  $\xi_t$





and

$$\tan \Delta\theta = \frac{\sigma_s}{R} \quad (2.23)$$

and taking into account that  $\sin \Delta\theta \approx \Delta\theta$  and  $\tan \Delta\theta \approx \Delta\theta$  as  $\Delta\theta \ll 1$ , the transversal coherence length can be derived:

$$\xi_t = \frac{\lambda R}{2\sigma_s} \quad (2.24)$$

Typically, the intensity profile of the beam is Gaussian shaped (Sinha et al. 2014) with the form

$$I(x, y) \propto \exp\left(-\frac{x^2}{2\sigma_x^2} - \frac{y^2}{2\sigma_y^2}\right), \quad (2.25)$$

which leads to two different transversal coherence lengths

$$\xi_{tx} = \frac{\lambda R}{2\sigma_{s_x}} \quad (2.26)$$

and

$$\xi_{ty} = \frac{\lambda R}{2\sigma_{s_y}}. \quad (2.27)$$

The coherence volume is defined as the volume spanned by the coherence lengths in all three spatial dimensions:

$$V_{\text{coh}} = \xi_{tx} \cdot \xi_{ty} \cdot \xi_l \quad (2.28)$$

At the coherence beamlines of the synchrotrons utilised in the course of this thesis,  $\xi_l$  was on the order of few microns while the transversal coherence lengths were on the order of 5–200  $\mu\text{m}$  (Sinha et al. 2014). Comparing to the maximum path length difference (see Eq. (2.21)) we can see that the longitudinal coherence length is typically smaller than the maximum path length difference. This implies that coherence is partially lost. However, as the maximum path length difference only accounts for the most extreme case, large parts of the illuminated sample volume still scatter coherently. To evaluate the degree of coherence of the scattered radiation, we can think of the sample as being composed of individual scattering volumes with volume  $V_{\text{coh}}$ , each scattering coherently. The degree of coherence, also called contrast factor, can be roughly estimated by

$$\beta \approx \frac{V'_{\text{coh}}}{V_{\text{illum}}}, \quad (2.29)$$

where  $V_{\text{illum}}$  is the total sample volume illuminated by the beam and  $V'_{\text{coh}}$  is the volume spanned by either the coherence length or the beam size in each dimension, whichever smaller. If the transversal coherence widths are larger than the beam diameter, this implies that

$$\beta \approx \frac{\xi_l}{W}. \quad (2.30)$$

The contrast can be approached more formally by considering the statistics of the scattered radiation. If the scattered radiation is fully coherent and the scattering amplitudes and phases are statistically independent, the probability distribution of the intensity of the resulting speckle patterns can be described by Eq. (2.31)

$$P(I) = \frac{e^{-I/\langle I \rangle}}{\langle I \rangle}, \quad (2.31)$$

where  $\langle I \rangle$  is the mean intensity (Goodman 2007). With the standard deviation  $\sigma = \sqrt{\langle I^2 \rangle - \langle I \rangle^2}$ , we obtain the contrast factor  $\beta = \sigma^2 / \langle I \rangle^2$ . We see that the contrast factor is unity for fully coherent radiation.

If we now have independently scattering subvolumes of the sample, the scattered radiation is only partially coherent and the statistics of the speckle intensities change accordingly. For  $M$  independent speckles in a continuous speckle pattern, the intensity distribution can be described by

$$P(I) = \left( \frac{MI}{\langle I \rangle} \right)^M \frac{e^{-MI/\langle I \rangle}}{\Gamma(M)I}, \quad (2.32)$$

with the gamma function  $\Gamma(M)$ . Now the standard deviation is  $\sigma = \langle I \rangle / \sqrt{M}$  and consequently the contrast factor is  $\beta = 1/M$ . We will see later on, that the SNR in the obtained intensity patterns is proportional to the contrast and come back to the contrast factor in Sect. 4.2.

## 2.2 Deducing Real-Space Time-Correlations from Intensity Pattern Series

As mentioned before, it is not possible to *directly* obtain real-space information from the scattering pattern. However, the changes in the pattern can be related to the changes which take place in real space. We will see how correlation functions can be used to describe these changes and to translate the intensity information into real-space information.

### 2.2.1 Van Hove Pair Correlation Function

Information about the dynamics of the particles of a material can be obtained by assessing the probability that a particle will be at  $\vec{r}$  at time  $t' + \Delta t$  given that a particle (the same or another) was at the origin at time  $t'$ . Formally, this can be written as

$$G(\vec{r}, \Delta t) = \left\langle \frac{1}{N} \sum_{a,b} \delta \left[ \vec{r} - \left( \vec{R}_a(t') - \vec{R}_b(t' + \Delta t) \right) \right] \right\rangle_{t'} \quad (2.33)$$

and is known as the van Hove pair correlation function. Here, the indices of summation  $a$  and  $b$  run over all  $N$  particles with position vectors  $\vec{R}_a$  and  $\vec{R}_b$ , but without summing over same indices (Hansen and McDonald 2006).

A very common function in dynamic light scattering is the so-called dynamic structure factor

$$S(\vec{q}, t) := \frac{1}{N} \sum_{a,b} \left\langle e^{i\vec{q} \cdot (\vec{R}_a(t') - \vec{R}_b(t' + t))} \right\rangle_{t'}, \quad (2.34)$$

with summation indices running over all particles.

We can see that this function is the Fourier transform of the van Hove pair correlation function:

$$\begin{aligned} S(\vec{q}, t) &= \frac{1}{N} \sum_{a,b} \int d\vec{r} \left\langle e^{i\vec{q} \cdot \vec{r}} \delta \left[ \vec{r} - \left( \vec{R}_a(t') - \vec{R}_b(t' + t) \right) \right] \right\rangle_{t'} \\ &= \int d\vec{r} e^{i\vec{q} \cdot \vec{r}} \left\langle \frac{1}{N} \sum_{a,b} \delta \left[ \vec{r} - \left( \vec{R}_a(t') - \vec{R}_b(t' + t) \right) \right] \right\rangle_{t'} \\ &= \int d\vec{r} e^{i\vec{q} \cdot \vec{r}} G(\vec{r}, t) \\ &= \mathcal{F}(G(\vec{r}, t)) \end{aligned} \quad (2.35)$$

Here it is disregarded that the original definition of the van Hove pair correlation function does not include summing over same indices. The dynamic structure factor is also known as intermediate scattering function. In XPCS it is not directly measurable. We will see that we can put it in context to the autocorrelation of the electrical field and in turn with the intensity.

### 2.2.2 Autocorrelation Functions

A generic time autocorrelation function can be seen as a generalisation of the time average:

$$\langle A(t)A(t + \Delta t) \rangle = \lim_{T \rightarrow \infty} \frac{1}{T} \int_{-\frac{T}{2}}^{\frac{T}{2}} dt A(t)A(t + \Delta t) \quad (2.36)$$

The dependence of the autocorrelation function on the time lag  $\Delta t$  is an indicator for how fast a signal decorrelates or in other words, how fast a pattern decays. We can see that the autocorrelation function will always start at  $\langle A^2 \rangle$  for  $\Delta t = 0$  and decay to  $\langle A \rangle^2$  for  $\Delta t \rightarrow \infty$ , as there should be no connection between a signal at one point in time and at another at a much later time, as we are looking at non-periodic signals (see Fig. 2.8). Typically, this dependence will follow some kind of exponential decay, as we will see later on.

An important function is the normalised autocorrelation function of the electrical field

$$g^{(1)}(\vec{q}, \Delta t) := \frac{\langle E(\vec{q}, t)E^*(\vec{q}, t + \Delta t) \rangle}{\langle E(\vec{q}, t)E^*(\vec{q}, t) \rangle}. \quad (2.37)$$

We can see that this function is connected to the van Hove pair correlation function via the dynamic structure factor:

$$\begin{aligned} g^{(1)}(\vec{q}, \Delta t) &= \frac{\left\langle \left( \sum_{i=1}^N a_i e^{i\vec{q}\vec{r}_i(t)} \right) \left( \sum_{j=1}^N a_j^* e^{-i\vec{q}\vec{r}_j(t+\Delta t)} \right) \right\rangle}{\left\langle \left( \sum_{i=1}^N a_i e^{i\vec{q}\vec{r}_i(t)} \right) \left( \sum_{j=1}^N a_j^* e^{-i\vec{q}\vec{r}_j(t)} \right) \right\rangle} \\ &= \frac{\left\langle \sum_{i,j} a_i a_j^* e^{i\vec{q}(\vec{r}_i(t) - \vec{r}_j(t+\Delta t))} \right\rangle}{\left\langle \sum_{i,j} a_i a_j^* e^{i\vec{q}(\vec{r}_i(t) - \vec{r}_j(t))} \right\rangle} \\ &= \frac{\sum_{i,j} \left\langle e^{i\vec{q}(\vec{r}_i(t) - \vec{r}_j(t+\Delta t))} \right\rangle a_i a_j^*}{\sum_{i,j} \left\langle e^{i\vec{q}(\vec{r}_i(t) - \vec{r}_j(t))} \right\rangle a_i a_j^*} \end{aligned} \quad (2.38)$$

For identical scattering lengths, this simplifies to

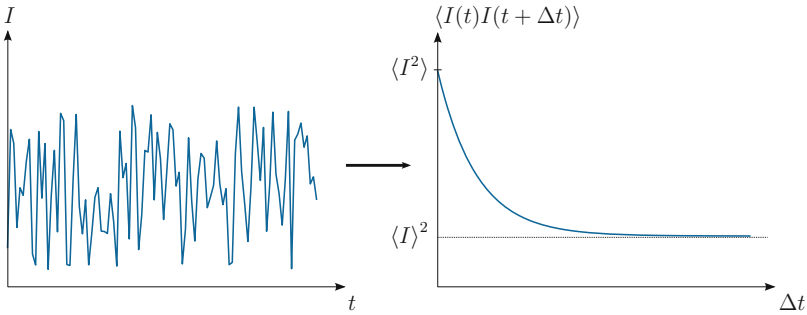


**Fig. 2.8** *Left* Scattered intensity from a diffusive process. *Right* The autocorrelation function of the scattering intensity decays from  $\langle I^2 \rangle$  to  $\langle I \rangle^2$  with increasing time lag  $\Delta t$

$$\begin{aligned}
g^{(1)}(\vec{q}, \Delta t) &= \frac{\sum_{i,j} \langle e^{i\vec{q}(\vec{r}_i(t) - \vec{r}_j(t + \Delta t))} \rangle}{\sum_{i,j} \langle e^{i\vec{q}(\vec{r}_i(t) - \vec{r}_j(t))} \rangle} \\
&= \frac{S(\vec{q}, t)}{S(\vec{q}, 0)}.
\end{aligned} \tag{2.39}$$

### 2.2.3 Link Between Autocorrelation Functions of Measured Intensities and Those of Real-Space Information

As we have seen, we can directly deduce the van Hove pair correlation function from  $g^{(1)}(\vec{q}, \Delta t)$ . As mentioned before, the electric field is not directly measurable. Instead, the intensity is experimentally obtained. We can link both dimensions using the normalised intensity autocorrelation function:

$$\begin{aligned}
g^{(2)}(\vec{q}, \Delta t) &:= \frac{\langle I(\vec{q}, t) I(\vec{q}, t + \Delta t) \rangle}{\langle I(\vec{q}, t) \rangle^2} \\
&= \frac{\langle E(\vec{q}, t) E^*(\vec{q}, t) E(\vec{q}, t + \Delta t) E^*(\vec{q}, t + \Delta t) \rangle}{\langle E(\vec{q}, t) E^*(\vec{q}, t) \rangle^2}
\end{aligned} \tag{2.40}$$

In the XPCS experiment, the time averaged time correlation function of the intensity is obtained. In equilibrated samples, the ergodic theorem should hold, claiming that the time average equals the ensemble average. This is true for systems where a representative fraction of states is reached within the measurement time.

The autocorrelation function can be simplified using Isserlis' theorem (Isserlis 1918), also known as Wick's theorem (Wick 1950), as the scattered amplitudes follow Gaussian statistics:

$$\begin{aligned}
&\langle E(\vec{q}, t) E^*(\vec{q}, t) E(\vec{q}, t + \Delta t) E^*(\vec{q}, t + \Delta t) \rangle \\
&= \langle E(\vec{q}, t) E^*(\vec{q}, t) \rangle \langle E(\vec{q}, t + \Delta t) E^*(\vec{q}, t + \Delta t) \rangle \\
&\quad + \langle E(\vec{q}, t) E(\vec{q}, t + \Delta t) \rangle \langle E^*(\vec{q}, t) E^*(\vec{q}, t + \Delta t) \rangle \\
&\quad + \langle E(\vec{q}, t) E^*(\vec{q}, t + \Delta t) \rangle \langle E^*(\vec{q}, t) E(\vec{q}, t + \Delta t) \rangle
\end{aligned} \tag{2.41}$$

With  $\langle EE \rangle \propto \langle e^{-i2\omega t} \rangle = 0$  and  $\langle E^* E^* \rangle \propto \langle e^{-i2\omega t} \rangle = 0$ , this simplifies to

$$\begin{aligned}
&\langle E(\vec{q}, t) E^*(\vec{q}, t) \rangle \langle E(\vec{q}, t + \Delta t) E^*(\vec{q}, t + \Delta t) \rangle \\
&\quad + \langle E(\vec{q}, t) E^*(\vec{q}, t + \Delta t) \rangle \langle E^*(\vec{q}, t) E(\vec{q}, t + \Delta t) \rangle \\
&= \langle E(\vec{q}, t) E^*(\vec{q}, t) \rangle^2 + \langle E(\vec{q}, t) E^*(\vec{q}, t + \Delta t) \rangle^2.
\end{aligned} \tag{2.42}$$

This can be used to connect  $g^{(1)}$  and  $g^{(2)}$ :

$$g^{(2)}(\vec{q}, \Delta t) = 1 + \left| \frac{\langle E(\vec{q}, t) E^*(\vec{q}, t + \Delta t) \rangle}{\langle E(\vec{q}, t) E^*(\vec{q}, t) \rangle} \right|^2 = 1 + |g^{(1)}(\vec{q}, \Delta t)|^2 \quad (2.43)$$

This connection is only true for perfect coherence under ideal conditions. In the experimental environment, the relation has to be slightly modified:

$$g^{(2)}(\vec{q}, \Delta t) = 1 + \beta |g^{(1)}(\vec{q}, \Delta t)|^2 \quad (2.44)$$

The factor  $\beta$  is called contrast (see Sect. 2.1.3) and also Siegert or coherence factor (Sutton 2008) and accounts for the fact that the used radiation is not perfectly coherent initially and also coherence is lost by optical elements of the setup. The coherence factor can be calculated for the optics of a given setup or experimentally obtained, measuring a sample with no dynamics. It can vary between 0 and 1 and decreases with increasing scattering angle (see Fig. 2.9).

## 2.3 Unravelling Atomic Dynamics

Now that we know how to obtain real-space correlations (namely  $g^{(1)}(\vec{q}, \Delta t)$ ), the autocorrelation of the electrical field), we can find models which are able to describe

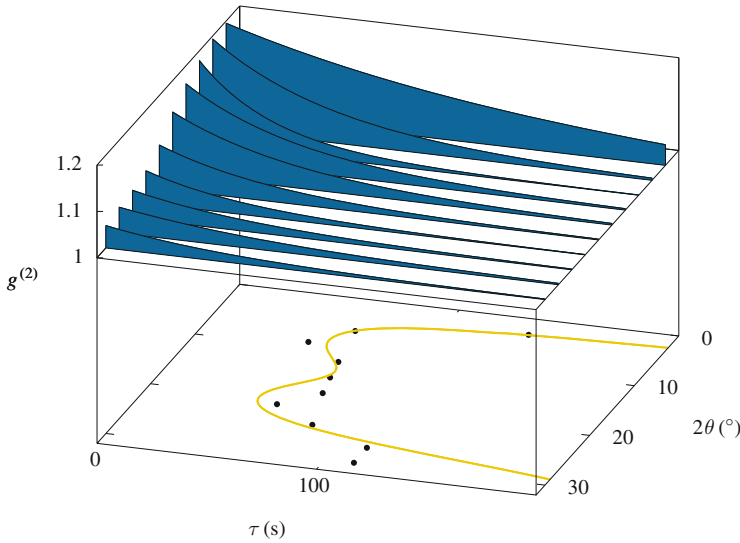


**Fig. 2.9** Dependence of the intensity autocorrelation function on scattering angle and time lag. The coherence factor of each measurement is the axis intercept of the according autocorrelation curve. The plot on the *bottom* of the graph shows the corresponding correlation times and a fit to these decay times

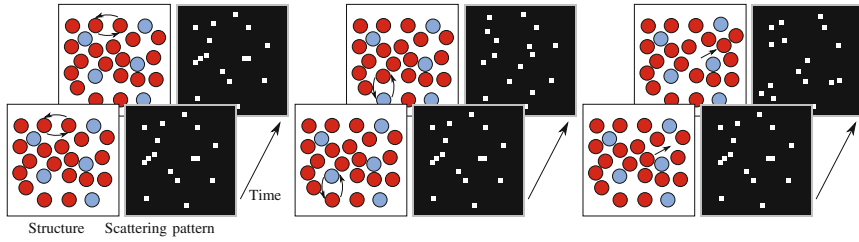


**Fig. 2.10** Detectable dynamics with aXPCS. Each column shows a structural change and the according scattering pattern over time. *Left* Two atoms of the same atomic species exchange positions. No change in scattering pattern occurs, thus this exchange is not detectable. *Middle* Exchange of two atoms of different elements. The scattering pattern changes and the exchange is detectable. *Right* Translation of an atom. The scattering pattern changes thus the movement of the atom is detectable

these correlations and provide deeper insight into the actual atomic dynamics. As shown in Fig. 2.10, aXPCS is not sensitive to all atomic movements. In fact it can be seen as a remarkable property of this method that it can be used to specifically focus on the translatory movement of atoms. It should be further noted that in the context of this thesis, the term *dynamics* describes solely diffusion and excludes other dynamic phenomena like e.g. phonons, which are taking place on entirely different time scales (see Fig. 1.3).

### 2.3.1 Continuous Diffusion

Assuming a continuous medium, the consequences of diffusion for the concentration of an atomic species can be described by Fick's laws. As the self-correlation function  $G_s$  can be seen as a representation of the particle concentration, it has to obey Fick's second law:

$$\frac{\partial G_s(\vec{r}, t)}{\partial t} = D \nabla^2 G_s(\vec{r}, t) \quad (2.45)$$

Here,  $D$  is called the self-diffusion coefficient. With  $G_s(\vec{r}, 0) = \delta(\vec{r})$  and assuming that the particle is followed over a longer range relative to the atomic distances, the solution of Eq. (2.45) is the Gaussian function:

$$G_s(\vec{r}, t) = \frac{1}{(4\pi Dt)^{3/2}} e^{-\frac{r^2}{4Dt}} \quad (2.46)$$

The mean square displacement of a particle can be expressed in terms of the diffusion coefficient:

$$\langle \vec{r}^2(t) \rangle := \int r^2 G_s(\vec{r}, t) d\vec{r} \quad (2.47)$$

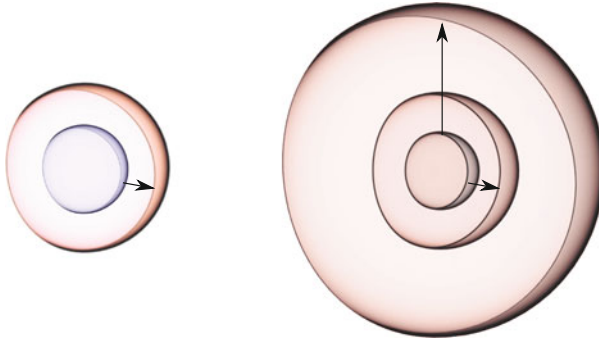


**Fig. 2.11** Visualisation of the fixed jump lengths and isotropic jump directions of the Chudley–Elliott model. *Left* Single jump Chudley–Elliott model. *Right* Two-jump Chudley–Elliott model

Solving this equation for isotropic media (i.e. in spherical coordinates) leads to

$$\langle \vec{r}^2(t) \rangle = \frac{4\pi}{(4\pi Dt)^{3/2}} \int_0^\infty r^4 e^{-\frac{r^2}{4Dt}} dr = 6Dt. \quad (2.48)$$

Following atomic motion on smaller scales relative to the atomic distances, the Gaussian approximation is not valid anymore. A microscopic model has to take into account the discretised nature of the atomic motion (Figs. 2.11 and 2.12).

### 2.3.2 Jump Diffusion: Chudley–Elliott Model

A mechanism which can describe atomic-scale transport is the so-called jump diffusion. It is based on the assumption that atoms stay at a fixed position most of the time, only vibrating around this position. Transport happens by very fast translatory motions, which are uncorrelated in time and so much faster than the time the atom spends at a fixed position (the so-called mean residence time  $\tau_0$ ), that these motions can be described as (quasi-instantaneous) jumps. Another model assumption is that the atomic jumps are isotropic and have the same specific distance. This model was first studied in detail by Chudley and Elliott (1961) who derived the van Hove pair correlation function for a diffusion process under these assumptions. The derivation is based on the master equation for the probability of finding an atom at position  $\vec{r}$ ,

$$\frac{\partial P(\vec{r}, t)}{\partial t} = -\frac{1}{\tau_0} P(\vec{r}, t) + \frac{1}{N\tau_0} \sum_j P(\vec{r} + \vec{r}_j, t), \quad (2.49)$$

where the index of summation  $j$  runs over all  $N$  potential positions  $\vec{r}_j$  the atom could jump from.

Setting  $G(\vec{r}, 0) = \delta(\vec{r})$ , this equation is solved by the van Hove pair correlation function. Introducing the Fourier transform



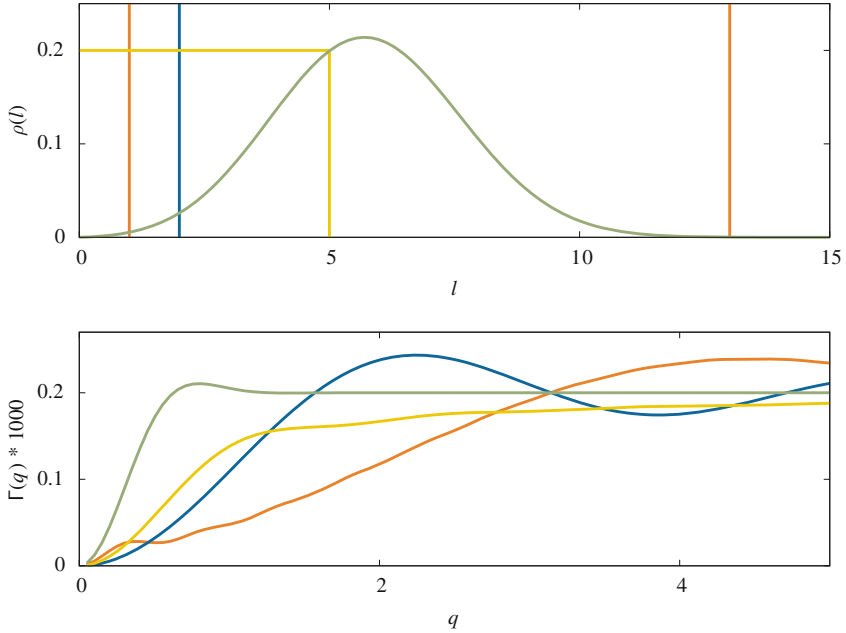


**Fig. 2.12** Jump length distributions (*upper plot*) and inverse correlation times (*lower plot*) for the single jump Chudley–Elliott model (*blue line*, parameter value  $l = 2$ ), the two-jump Chudley–Elliott model (*orange line*, parameter values  $l_1 = 1, l_2 = 13, \omega_1 = 0.9$ ), the Jobic model (*green line*,  $d_0 = 5, r_0 = 2$ ) and for uniformly distributed jumps (*yellow line*,  $l_{\max} = 5$ ). All inverse correlation times were plotted using  $\tau_0^{-1} = 2 \times 10^{-4}$

$$P(\vec{r}, t) = \int \tilde{P}(\vec{q}, t) e^{-i\vec{q}\vec{r}} d\vec{q} \quad (2.50)$$

and rewriting the master equation accordingly leads to a differential equation:

$$\frac{\partial \left( \int \tilde{P}(\vec{q}, t) e^{-i\vec{q}\vec{r}} d\vec{q} \right)}{\partial t} = -\frac{1}{\tau_0} \int \tilde{P}(\vec{q}, t) e^{-i\vec{q}\vec{r}} d\vec{q} + \frac{1}{N\tau_0} \sum_j \int \tilde{P}(\vec{q}, t) e^{-i\vec{q}(\vec{r} + \vec{r}_j)} d\vec{q} \quad (2.51)$$

This equation can be solved by an exponential decay function. Setting

$$\tilde{P}(\vec{q}, t) = e^{-\Gamma(\vec{q})t}, \quad (2.52)$$

the equation reads

$$\frac{\partial \left( \int e^{-\Gamma(\vec{q})t - i\vec{q}\vec{r}} d\vec{q} \right)}{\partial t} = -\frac{1}{\tau_0} \int e^{-\Gamma(\vec{q})t - i\vec{q}\vec{r}} d\vec{q} + \frac{1}{N\tau_0} \sum_j \int e^{-\Gamma(\vec{q})t - i\vec{q}(\vec{r} + \vec{r}_j)} d\vec{q}. \quad (2.53)$$

The decay parameter  $\Gamma(\vec{q})$  is also known as inverse correlation time  $\tau^{-1}$  or line width. After differentiating, we get:

$$\begin{aligned}
 \int (-\Gamma(\vec{q})) e^{-\Gamma(\vec{q})t - i\vec{q}\vec{r}} d\vec{q} &= -\frac{1}{\tau_0} \int e^{-\Gamma(\vec{q})t - i\vec{q}\vec{r}} d\vec{q} + \frac{1}{N\tau_0} \sum_j \int e^{-\Gamma(\vec{q})t - i\vec{q}\vec{r}} \cdot e^{-i\vec{q}\vec{r}_j} d\vec{q} \\
 &= -\frac{1}{\tau_0} \int e^{-\Gamma(\vec{q})t - i\vec{q}\vec{r}} d\vec{q} + \frac{1}{N\tau_0} \sum_j \int e^{-\Gamma(\vec{q})t - i\vec{q}\vec{r}} \cdot e^{-i\vec{q}\vec{r}_j} d\vec{q} \\
 &= \int \left( -\frac{1}{\tau_0} + \frac{1}{N\tau_0} \sum_j e^{-i\vec{q}\vec{r}_j} \right) e^{-\Gamma(\vec{q})t - i\vec{q}\vec{r}} d\vec{q}
 \end{aligned} \tag{2.54}$$

Thus we obtain a solution for the functional dependence of the decay on the scattering vector:

$$\Gamma(\vec{q}) = \frac{1}{N\tau_0} \sum_j \left( 1 - e^{i\vec{q}\vec{r}_j} \right) \tag{2.55}$$

Now we can link the autocorrelation functions to the scattering vector:

$$g^{(1)}(\vec{q}, \Delta t) = \frac{S(\vec{q}, \Delta t)}{S(\vec{q}, 0)} = \frac{\mathcal{F}(G(\vec{r}, \Delta t))}{\mathcal{F}(G(\vec{r}, 0))} = \frac{\tilde{P}(\vec{q}, \Delta t)}{\tilde{P}(\vec{q}, 0)} = e^{-\Gamma(\vec{q})\Delta t} \tag{2.56}$$

$$g^{(2)}(\vec{q}, \Delta t) = 1 + \beta |g^{(1)}|^2 = 1 + \beta e^{-2\Gamma(\vec{q})\Delta t} \tag{2.57}$$

Taking into account the model assumption of a fixed jump length  $l$  and an isotropic jump distribution, we can rewrite  $\Gamma(\vec{q})$  in integral form:

$$\Gamma(q) = \frac{1}{\tau_0} \frac{\int_0^{2\pi} \int_0^\pi (1 - e^{iq l \cos \theta}) \sin \theta d\theta d\phi}{\int_0^{2\pi} \int_0^\pi \sin \theta d\theta d\phi} \tag{2.58}$$

Substituting  $u = \cos \theta$  and using  $\frac{e^{iq l} - e^{-iq l}}{2i} = \sin(q l)$ , we obtain the single jump Chudley–Elliott form:

$$\begin{aligned}
 \Gamma(q) &= \frac{1}{\tau_0} \frac{2\pi \int_{-1}^1 (1 - e^{iq l u}) du}{4\pi} \\
 &= \frac{1}{2\tau_0} \left( 2 - \frac{e^{iq l} - e^{-iq l}}{iq l} \right) \\
 &= \frac{1}{\tau_0} \left( 1 - \frac{\sin(q l)}{q l} \right)
 \end{aligned} \tag{2.59}$$

In the limit of very small angles (or more precisely  $q l \ll 1$ ), the sine function can be expanded and the inverse correlation time  $\Gamma(q)$  simplifies to

$$\lim_{(ql) \rightarrow 0} \Gamma(q) = \frac{1}{\tau_0} \left( 1 - \frac{ql - \frac{(ql)^3}{3!} + \dots}{ql} \right) \approx \frac{q^2 l^2}{6\tau_0}, \quad (2.60)$$

often described in the form  $\Gamma(q) = Dq^2$ , where  $D$  is called diffusion coefficient.

Keeping the criterion of isotropic jumps but relaxing the criterion of a single jump length, Eq. (2.59) can be generalised (Jobic 2000). Using a jump length distribution  $\rho(l)$ , Eq. (2.59) can be rewritten in the form

$$\Gamma(q) = \frac{1}{\tau_0} \frac{\int \left( 1 - \frac{\sin(ql)}{ql} \right) \rho(l) dl}{\int \rho(l) dl}. \quad (2.61)$$

If  $\rho(l)$  is normalised, this simplifies to

$$\Gamma(q) = \frac{1}{\tau_0} \left( 1 - \int_0^\infty \frac{\sin(ql)}{ql} \rho(l) dl \right). \quad (2.62)$$

### 2.3.3 Extensions of the Chudley–Elliott Model

We can use the results obtained by the generalisation shown in Eq. (2.62) to derive  $\Gamma(q)$  for other jump geometries.

#### Uniformly Distributed Jumps

The Chudley–Elliott model is one extreme of jump distributions, assuming that only one jump distance is possible. Another extreme can be constructed assuming that all jump lengths up to a certain distance are equally probable:

$$\rho(l) = \begin{cases} \frac{1}{l_{\max}} & 0 < l < l_{\max} \\ 0 & \text{otherwise} \end{cases} \quad (2.63)$$

This leads to

$$\begin{aligned} \Gamma(q) &= \frac{1}{\tau_0} \left( 1 - \frac{1}{l_{\max}} \int_0^{l_{\max}} \frac{\sin(ql)}{ql} dl \right) \\ &= \frac{1}{\tau_0} \left( 1 - \frac{1}{l_{\max}} \frac{\text{Si}(ql_{\max})}{q} \right), \end{aligned} \quad (2.64)$$

where the sine integral  $\text{Si}(x)$  can be calculated numerically or approximated by a truncated series expansion.

### Jobic Model

Jobic (2000) introduced a jump length distribution similar to a model proposed by Hall and Ross (1981). In this model, the jump lengths follow the distribution

$$\rho(l) = \frac{l}{d_0 r_0 \sqrt{2\pi}} \exp\left(-\frac{(l - d_0)^2}{2r_0^2}\right). \quad (2.65)$$

Here,  $d_0$  represents the jump distance and  $r_0$  the delocalisation of an atom from its site. The inverse correlation time is then given by

$$\begin{aligned} \Gamma(q) &= \frac{1}{\tau_0} \left( 1 - \frac{1}{qd_0 r_0 \sqrt{2\pi}} \int_0^\infty \sin(ql) \exp\left(-\frac{(l - d_0)^2}{2r_0^2}\right) dl \right) \\ &= \frac{1}{\tau_0} \left( 1 - \frac{\sin(qd_0)}{qd_0} \exp\left(-\frac{q^2 r_0^2}{2}\right) \right). \end{aligned} \quad (2.66)$$

### Two-Jump Chudley–Elliott Model

A straightforward way to allow for more than one jump distance imposed by the Chudley–Elliott model is to include a second independent jump. This can be achieved with the following jump distribution:

$$\rho(l) = \omega_1 \delta(l - l_1) + \omega_2 \delta(l - l_2) \quad (2.67)$$

with the relative weights  $\omega_i$  of the jump lengths  $l_i$ , where  $\omega_1 + \omega_2 = 1$ . With this distribution, the inverse correlation time takes the form

$$\Gamma(q) = \frac{1}{\tau_0} \left( 1 - \omega_1 \frac{\sin(ql_1)}{ql_1} - (1 - \omega_1) \frac{\sin(ql_2)}{ql_2} \right). \quad (2.68)$$

## 2.4 Applying aXPCS to Diffusion in Glasses

Studying atomic diffusion in glasses compared to diffusion in crystals poses additional challenges as the structure is much less defined and the underlying mechanisms of diffusion are much less clear. We will have a look at some effects typically encountered when studying glasses and see how they influence the way the dynamics can be described.

### 2.4.1 Influence of Different Scattering Species

In contrast to crystalline materials, glasses do not show a distinct long-range order which would result in a Bragg peak. Instead, a broad distribution of scattering

intensity is observed. This poses additional challenge to interpreting aXPCS data, as the scattered intensity of the rather immobile matrix can not be easily separated from the scattering of the diffusing atoms under consideration. In principle, the measured intensity (also called structure factor) can be represented by the weighted sum of partial structure factors (Soper 2005)

$$S(q) = \sum_{\alpha, \beta \geq \alpha} (2 - \delta_{\alpha\beta}) c_{\alpha} c_{\beta} f_{\alpha} f_{\beta} S_{\alpha\beta}(q), \quad (2.69)$$

where  $c_{\alpha}$  is the atomic fraction of species  $\alpha$  and  $f_{\alpha}$  is the scattering length.

In some cases, like in lead silicate glass (see Chap. 5), the huge difference in scattering strength of the lead atom compared to Si and O allows to interpret the measurements like a system of one element species. Thus we can follow mainly Pb atoms in their movement and neglect the other atoms in the sample. This is one of the reasons why lead silicate glass is an ideal candidate as a starting point for studying atomic diffusion in glasses.

### 2.4.2 Kohlrausch Exponent

A pure exponential decay as derived in Eq.(2.57) can often only be observed in aXPCS experiments when a single process is active. When multiple dynamic processes with similar decay rates are observed at the same time (e.g. when in some regions atoms move with different diffusion rates than in the other regions of the material, see Fig. 2.13), they cannot be easily separated. Instead, the stretching parameter

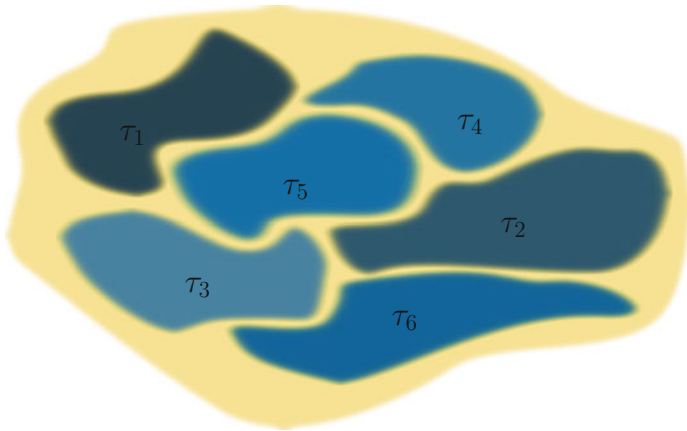


**Fig. 2.13** Visualisation of a glass sample with different regions distinguished by the mean residence time which is predominant in each region. Due to macroscopic ageing, parts of the sample can be in different evolution levels of the dynamics. Thus the same type of process can be unchanged over the measurement time but have spatially different diffusion speeds

$\alpha$ , also called KWW parameter, can be used. This empirical parameter has been introduced in the 19th century by Kohlrausch and resurrected by Williams and Watts (1970) and can be seen as a straightforward approximation for the sum of multiple exponentials. With this approximation, the intensity autocorrelation function takes the form

$$g^{(2)}(\vec{q}, \Delta t) = 1 + \beta e^{-2(\Gamma(\vec{q})\Delta t)^\alpha}, \quad (2.70)$$

with the inverse correlation time  $\Gamma(\vec{q}) = \frac{1}{\tau(\vec{q})}$ .

A value of  $\alpha = 1$  just leads to the normal behaviour derived in Eq.(2.57). In Fig. 2.14, the effect of applying the KWW function is shown. The stretching parameter  $\alpha$  can be less than one (in that case, the KWW function is also called stretched exponential function) for constrained or subdiffusive motion of particles (Pontoni et al. 2003; Guo et al. 2012) or for dynamics where several processes are active. A value of  $\alpha > 1$  (where the KWW function is also called compressed exponential function) can indicate non-equilibrium dynamics (Madsen et al. 2010; Leitner et al. 2012; Ruta et al. 2012).

### 2.4.3 Short-Range Order Correction

As we have seen, the measured  $q$  dependence of the correlation time allows to test mathematical models of different diffusion processes. We have also seen that aXPCS

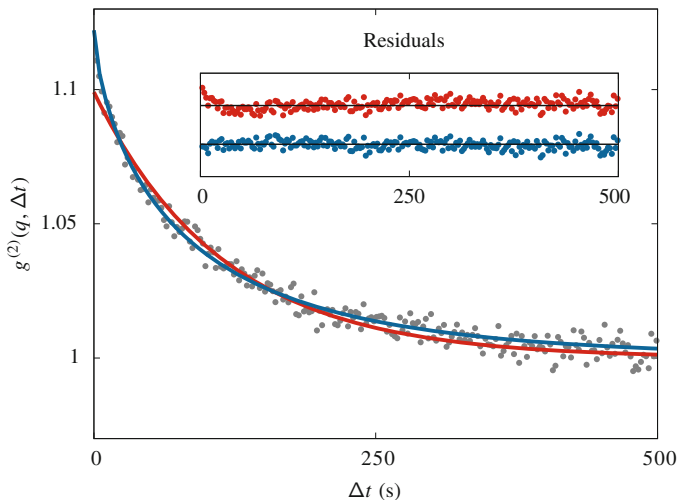


**Fig. 2.14** Comparison of the autocorrelation function of experimental intensity values and residuals using the KWW function with different KWW parameters. In the main plot, the *red line* depicts the pure exponential decay with  $\alpha = 1$ , while the *blue line* is a fit of the KWW function with  $\alpha < 1$  to the data. The *inset* shows the residuals which are the subtraction of the fitted curve from the data points. The stretched exponential decay function clearly fits the data better than the pure exponential decay

is a coherent method or in other words, it takes into account the diffusion of all atoms rather than following one single atom only.

In addition to the scattering described so far, there are further effects which influence the intensity due to the short-range order. This spatial correlation of the diffusing atoms to other atoms in their direct vicinity typically results in a broad intensity peak, the so-called structure peak. This effect is known as the de Gennes narrowing, first described qualitatively for coherent QENS (De Gennes 1959). It basically states that those species whose dynamics are slower than the dynamics of other diffusing species will form longer-living structures, which will in turn lead to a higher scattering intensity in the  $q$  range corresponding to the size of these structures. Thus the  $q$  dependence of the scattering intensity  $S_{\text{SRO}}(\vec{q})$  gives additional information on the diffusion rate of atoms in the material.

The diffusion models described before are in fact valid for incoherent methods and have to be modified for a coherent method like aXPCS if the system studied is ordered. The diffuse scattering under short-range order has been investigated in a linear approximation by Sinha and Ross (1988) and is discussed in detail in Leitner and Vogl (2011). For a weak short-range ordering, the coherent inverse correlation time can be described in terms of the incoherent inverse correlation time:

$$\tau_{\text{coh}}^{-1}(\vec{q}) = \frac{\tau_{\text{inc}}^{-1}(\vec{q})}{S_{\text{SRO}}(\vec{q})} \quad (2.71)$$

This correlation time  $\tau_{\text{coh}}$  can now be compared with the results of coherent experiments, where  $\tau_{\text{inc}}(\vec{q})$  is the correlation time which would be obtained with an incoherent scattering method.

## References

- Abernathy, D. L., Grübel, G., Brauer, S., McNulty, I., Stephenson, G. B., Mochrie, S. G. J., et al. (1998). Small-angle X-ray scattering using coherent undulator radiation at the ESRF. *Journal of Synchrotron Radiation*, 5 (Part 1), 37–47.
- Chudley, C. T., & Elliott, R. J. (1961). Neutron scattering from a liquid on a jump diffusion model. *Proceedings of the Physical Society London*, 77(2), 353–361.
- De Gennes, P. G. (1959). Liquid dynamics and inelastic scattering of neutrons. *Physica*, 25(7–12), 825–839.
- Goodman, J. W. (2007). *Speckle phenomena in optics: theory and applications*. Englewood: Roberts & Company.
- Guo, H., Bourret, G., Lennox, R. B., Sutton, M., Harden, J. L., & Leheny, R. L. (2012). Entanglement-controlled subdiffusion of nanoparticles within concentrated polymer solutions. *Physical Review Letters*, 109(5), 055901.
- Hall, P. L., & Ross, D. K. (1981). Incoherent neutron scattering functions for random jump diffusion in bounded and infinite media. *Molecular Physics*, 42(3), 673–682.
- Hansen, J.-P., & McDonald, I. R. (2006). *Theory of simple liquids*. London: Elsevier.
- Isserlis, L. (1918). On a formula for the product-moment coefficient of any order of a normal frequency distribution in any number of variables. *Biometrika*, 12(1–2), 134–139.

- Jobic, H. (2000). Diffusion studies using quasi-elastic neutron scattering. In N. K. Kanellopoulos (Ed.), *Recent advances in gas separation by microporous ceramic membranes* (Vol. 6, pp. 109–137). Amsterdam: Elsevier.
- Leitner, M., & Vogl, G. (2011). Quasi-elastic scattering under short-range order: the linear regime and beyond. *Journal of Physics: Condensed Matter*, 23(25), 254206.
- Leitner, M., Sepiol, B., Stadler, L.-M., & Pfau, B. (2012). Time-resolved study of the crystallization dynamics in a metallic glass. *Physical Review B*, 86(6), 064202.
- Madsen, A., Leheny, R. L., Guo, H., Sprung, M., & Czakkel, O. (2010). Beyond simple exponential correlation functions and equilibrium dynamics in x-ray photon correlation spectroscopy. *New Journal of Physics*, 12(5), 055001.
- Marchesini, S., He, H., Chapman, H. N., Hau-Riege, S. P., Noy, A., Howells, M. R., et al. (2003). X-ray image reconstruction from a diffraction pattern alone. *Physical Review B*, 68(14), 140101.
- Pontoni, D., Narayanan, T., Petit, J.-M., Grübel, G., & Beysens, D. (2003). Microstructure and dynamics near an attractive colloidal glass transition. *Physical Review Letters*, 90(18), 188301.
- Ruta, B., Chushkin, Y., Monaco, G., Cipelletti, L., Pineda, E., Bruna, P., et al. (2012). Atomic-scale relaxation dynamics and aging in a metallic glass probed by x-ray photon correlation spectroscopy. *Physical Review Letters*, 109, 165701.
- Sandy, A. R., Lurio, L. B., Mochrie, S. G. J., Malik, A., Stephenson, G. B., Pelletier, J. F., et al. (1999). Design and characterization of an undulator beamline optimized for small-angle coherent x-ray scattering at the advanced photon source. *Journal of Synchrotron Radiation*, 6(6), 1174–1184.
- Sinha, S. K., & Ross, D. K. (1988). Self-consistent density response function method for dynamics of light interstitials in crystals. *Physica B*, 149(1–3), 51–56.
- Sinha, S. K., Jiang, Z., & Lurio, L. B. (2014). X-ray photon correlation spectroscopy studies of surfaces and thin films. *Advanced Materials*, 26(46), 7764–7785.
- Soper, A. (2005). Partial structure factors from disordered materials diffraction data: An approach using empirical potential structure refinement. *Physical Review B*, 72(10), 104204.
- Sutton, M. (2006). X-ray intensity fluctuation spectroscopy. In F. Hippert, E. Geissler, J. L. Hodeau, E. Lelièvre-Berna, & J.-R. Regnard (Eds.), *Neutron and x-ray spectroscopy* (pp. 297–318). Dordrecht: Springer.
- Sutton, M. (2008). A review of x-ray intensity fluctuation spectroscopy. *Comptes Rendus Physique*, 9(5–6), 657–667.
- Wick, G. (1950). The evaluation of the collision matrix. *Physical Review*, 80(2), 268–272.
- Williams, G., & Watts, D. C. (1970). Non-symmetrical dielectric relaxation behaviour arising from a simple empirical decay function. *Transactions of the Faraday Society*, 66, 80.



Atomic Diffusion in Glasses Studied with Coherent  
X-Rays

Ross, M.

2016, XVIII, 111 p. 67 illus., 22 illus. in color., Hardcover

ISBN: 978-3-319-28644-0